Analysis of Heterogeneously Catalyzed Reactions Close to Bubbles

Jodi A. Raffensberger, Benjamin J. Glasser, and Johannes G. Khinast
Dept. of Chemical and Biochemical Engineering, Rutgers University, Piscataway, NJ 08854

DOI 10.1002/aic.10445
Published online March 30, 2005 in Wiley InterScience (www.interscience.wiley.com).

The objective of this work is to use numerical simulations to show how bubble (size and shape) and particle properties can influence the selectivity of fast heterogeneously catalyzed gas–liquid reactions. For fast gas–liquid–solid reactions, the reaction occurs primarily in the wake of the bubble and is thus dependent only on the mixing in this region. This work investigates how the wake structure changes for different bubble shapes and how catalyst particles distribute for different Stokes number particles. Finally, the results of this work will be applied to two industrially relevant reaction systems to show how choosing the correct design and operating parameters of a system can significantly influence the selectivity of fast heterogeneously catalyzed gas–liquid reactions. © 2005 American Institute of Chemical Engineers *AIChE J,* 51: 1482–1496, 2005
Keywords: bubble dynamics, selectivity, Euler-Lagrange simulation, catalysis, bubble phenomena, particulate flows

Introduction

Heterogeneously catalyzed gas–liquid reactions, such as hydrogenations, oxidations, or hydroformylations, are frequently carried out in bubble slurry reactors.[1,2] In these reactors, fine catalyst particles, with a typical diameter between 1 and 100 μm, are suspended in the liquid phase. Mixing and catalyst suspension are provided by injecting gas at the bottom of the reactor, which leads to a complicated mixing flow in the column. The advantages of bubble slurry reactors over fixed-bed reactors are that the temperature is more easily controlled and that fast reactions can be carried out with small catalyst particles, giving effectiveness factors close to one. A reactive gas (such as H_2, O_2, Cl_2) is sparged into the reactor and is then transported from the gas–liquid interface into the bulk liquid before being adsorbed onto the surface of the catalyst particles. In the case of fast reactions, however, the bulk concentration of the dissolved gas approaches zero (gas–liquid mass-transfer limitation). Therefore, only catalyst particles close to the gas–liquid interface participate in the reactions.[3]

Correspondence concerning this article should be addressed to J. G. Khinast at khinast@sol.rutgers.edu.

In a recent investigation on uncatalyzed gas–liquid reactions,[4] it was shown that fast reactions occur close to the bubble interface, and that the local mixing strongly influences the product distribution in the case of mixing-sensitive reaction networks. Mixing near the gas–liquid interface of a rising bubble is a function of the bubble size and shape and other system properties. Different flow regimes can develop, such as a closed wake with and without recirculation or periodic vortex shedding.[5] A parallel–consecutive reaction system was used to demonstrate that the different flow regimes affect the residence time of reactants and products in the wake of the bubble and will thus influence the product composition.[4] For example, if recirculation occurs in the wake of the bubble, the transport of fresh liquid reactant into the recirculation zone occurs only by diffusion, leading to reactant depletion. Furthermore, the residence time of the product in the recirculation zone is high, and thus the product will overreact to form undesired by-products (such as overhydrogenated compounds), resulting in poor yield and selectivity. If recirculation is not present in the wake or vortex shedding occurs, the dissolved gas is transported into regions rich in the liquid reactant and the product is quickly removed from the bubble, resulting in higher selectivity.

A study by Raffensberger et al.[6] expanded on this work and included the effect of heterogeneous catalyst particles, effec-

tively extending the earlier study to three-phase reactive flows. It was shown that the catalyst concentrates in different regions behind the bubble, depending on the particle Stokes and bubble Reynolds numbers. Because the effective reaction rate is a function of both the dissolved gas concentration and the catalyst concentration, the selectivity of the reaction depends on both the location of the solid catalyst and the local concentration of the dissolved gas.

The current study builds on this work as we attempt a much more detailed investigation of heterogeneously catalyzed reactions close to the gas–liquid interface by focusing on the flow and catalyst density distributions in the vicinity of the bubble. The combined results for the dissolved gas concentration fields, fluid motion, and catalyst distribution are then used to compute statistical properties, such as the instantaneous and average particle dispersion and a correlation coefficient, which allow us to predict the impact of bubble and catalyst characteristics on the yield and selectivity of fast gas–liquid reactions.

Although our studies[4,6,7] were the first to address the impact of micromixing on the selectivity of fast gas–liquid and gas–liquid–solid reactions, other groups have investigated in detail both micromixing phenomena and particle flow around objects immersed in a continuous phase. Micromixing has been the subject of many experimental and numerical studies, including miscible liquid reactions in stirred-tank reactors.[8-15] Investigation of particle motion and segregation has also been the subject of numerous numerical and experimental studies. Tang et al.[16] presented numerical results showing particle dispersion downstream of a bluff body. They found that intermediate Stokes number particles were dispersed into highly organized patterns. Yang et al.[17] experimentally validated the work by Tang et al. by investigating the flow of low and intermediate Stokes number particles in the wake behind a circular cylinder. In their work, the smaller particles (low Stokes number) traced the flow closely, whereas the intermediate sized particles had large radial components and demarcated the vortex patterns of the flow.

Chein and Chung[18] simulated particle dispersion in a fully developed two-dimensional (2-D) two-fluid mixing layer and found that the particle dispersion is strongly dependent on the particle Stokes number. By using "tagged" particles, they were able to compute the rate at which particles of various sizes dispersed relative to the fluid. Small particles tend to disperse at the same rate as the fluid, whereas large particles disperse much faster due to their inertia. Froncioni et al.[19] numerically studied the mixing in the time-dependent viscous wake behind a cylinder in air. By performing a stretching analysis, they were able to show that the fluid particles mix efficiently. However, even with the efficient mixing of the fluid, the solid particles tended to segregate according to their Stokes number with the lightest particles concentrating in the vortex cores, the intermediate particles in the vortex boundaries and the heaviest ones outside the vortical structures.

Several researchers have also studied the motion of solid particles in gas–liquid systems to determine particle adhesion and subsequent enhancement of the mass transfer rate. In an experimental study, Roizard et al.[20] investigated the flow of particles around a single gas bubble in both a stagnant fluid and in a laminar flow field. In the stagnant system, the particles either partially or totally covered the bubble formed at the tip of a needle, depending on the pH and ionic strength of the liquid phase. In nonstagnant systems, however, they concluded that particle adhesion forces were small, relative to the buoyancy and gravitational forces, regardless of pH and ionic strength of the fluid. Particles either slid or traveled around the bubble surface and did not adhere. Van der Zon et al.[21] improved on the nonstagnant experimental setup of Roizard et al.[20] and found that particle adhesion on bubbles was present in both stagnant and nonstagnant systems. In their experiments bubbles traveled through a slurry of particles, thus enforcing bubble–particle contact for small particles. They concluded that the particle adhesion was strongly affected by the composition of the gas phase, as well as the particle size and the interfacial tension between the gas and the liquid. As noted above, several researchers have shown both experimentally and numerically how particle adhesion at the bubble surface enhances the gas–liquid mass transfer rate.[3,22]

In the next section of this work, the modeling approach is described, followed by a discussion of the numerical implementation and the analysis. The hydrodynamic results with a corresponding statistical analysis are presented in the fourth section. The final part of this paper provides two examples illustrating the impact of catalyst particles on the selectivity of fast heterogeneous catalyzed gas–liquid reactions.

Model

Studying fast three-phase reactions close to gas bubbles in the presence of solid catalyst particles requires the understanding of both the hydrodynamic behavior of gas bubbles in a slurry and the motion of solid catalyst particles. Khinast[4] previously developed a hydrodynamic model for a single gas bubble rising in an infinite liquid medium. In the model, the bubble is assumed to be a stationary object (with perfect slip at the interface) with the fluid flowing past it at the terminal velocity. Furthermore, the bubble rises in a straight path, with its size and shape remaining constant. The model equations are transformed into elliptical coordinates as described by Khinast[4] and are made dimensionless by using half the interfocal distance a as the characteristic length and the terminal velocity U_∞ as the characteristic velocity. The dimensionless variables are

$$t = \frac{\hat{t}U_\infty}{a} \qquad P = \frac{\hat{P}}{U_\infty^2 \rho} \qquad u = \frac{\hat{u}}{U_\infty} \qquad v = \frac{\hat{v}}{U_\infty} \tag{1}$$

where u and v are the two dimensionless velocities in the η and φ directions, respectively. The continuity and Navier–Stokes equations in 2-D elliptical, conformal, orthogonal coordinates are

$$\frac{\partial (hu)}{\partial \eta} + \frac{\partial (hv)}{\partial \varphi} = 0 \tag{2}$$

$$\frac{\partial u}{\partial t} + \frac{u}{h}\frac{\partial u}{\partial \eta} + \frac{v}{h}\frac{\partial u}{\partial \varphi} - \frac{v^2}{h^2}h_\eta + \frac{uv}{h^2}h_\varphi = -\frac{1}{h}\frac{\partial P}{\partial \eta} + \frac{1}{\widetilde{\mathrm{Re}} \cdot h}\left[\frac{\partial}{\partial \eta}\left(\frac{1}{h^2}\frac{\partial hu}{\partial \eta}\right) + \frac{\partial}{\partial \varphi}\left(\frac{1}{h^2}\frac{\partial hu}{\partial \varphi}\right) - \frac{2}{h^3}\left(h_\eta \frac{\partial hv}{\partial \varphi} - h_\varphi \frac{\partial hv}{\partial \eta}\right)\right] \tag{3}$$

$$\frac{\partial v}{\partial t}+\frac{u}{h}\frac{\partial v}{\partial \eta}+\frac{v}{h}\frac{\partial v}{\partial \varphi}+\frac{uv}{h^2}h_\eta-\frac{u^2}{h^2}h_\varphi=-\frac{1}{h}\frac{\partial P}{\partial \varphi}+\frac{1}{\widehat{\mathrm{Re}}\cdot h}\left[\frac{\partial}{\partial \eta}\left(\frac{1}{h^2}\frac{\partial hv}{\partial \eta}\right)+\frac{\partial}{\partial \varphi}\left(\frac{1}{h^2}\frac{\partial hv}{\partial \varphi}\right)-\frac{2}{h^3}\left(h_\varphi\frac{\partial hu}{\partial \eta}-h_\eta\frac{\partial hu}{\partial \varphi}\right)\right] \quad (4)$$

where

$$h=\frac{H}{a}=\sqrt{\cosh^2\eta-\sin^2\varphi} \qquad h_\eta=\frac{\partial h}{\partial \eta}=\frac{\sinh\eta\cosh\eta}{h} \qquad h_\varphi=\frac{\partial h}{\partial \varphi}=-\frac{\sin\varphi\cos\varphi}{h} \quad (5)$$

Boundary conditions at the gas–liquid interface and at the inflow and outflow domain are described elsewhere.[4] The Reynolds number (Re) is based on the major axis of the ellipse and is expressed as

$$\mathrm{Re}=2\cosh\eta_0\frac{aU_\infty\rho}{\mu}=2\cosh\eta_0\widehat{\mathrm{Re}} \quad (6)$$

In Eq. 6 the viscosity is the "effective slurry viscosity," using the assumption that a slurry can be treated as a viscous liquid, which is justified at low solid holdups.[23]

The motion of small circular solid particles in a flow can be described by the Maxey–Riley model based on Newton's second law,[24] as follows

$$m_p\frac{d\mathbf{u}_p}{d\hat{t}}=(m_p-m_f)\mathbf{g}+m_f\frac{D\mathbf{u}}{D\hat{t}}\bigg|_{\mathbf{x}(t)}-\frac{1}{2}m_f\frac{d}{d\hat{t}}\left\{\mathbf{u}_p(\hat{t})-\mathbf{u}[\mathbf{x}(\hat{t}),\hat{t}]-\frac{1}{10}\hat{a}_p^2\nabla^2\mathbf{u}|_{\mathbf{x}(\hat{t})}\right\}-6\pi\hat{a}_p\mu\left\{\mathbf{u}_p(\hat{t})-\mathbf{u}(\mathbf{x}(\hat{t}),\hat{t})-\frac{1}{6}\hat{a}_p^2\nabla^2\mathbf{u}|_{\mathbf{x}(\hat{t})}\right\}-6\pi\hat{a}_p^2\mu\int_0^{\hat{t}}\frac{d\left\{\mathbf{u}_p(\tau)-\mathbf{u}(\mathbf{x}(\tau),\tau)-\frac{1}{6}\hat{a}_p^2\nabla^2\mathbf{u}|_{\mathbf{x}(\tau)}\right\}\Big/d\tau}{\sqrt{\pi\nu(\hat{t}-\tau)}}d\tau \quad (7)$$

where $\mathbf{u}=(\hat{u},\hat{v})^T$ is the fluid velocity, $\mathbf{u}_p=(\hat{u}_p,\hat{v}_p)^T$ is the particle velocity, $\hat{a}_p$ is the particle radius, $\hat{t}$ is dimensional time; m_p and m_f are the mass of the particle and the displaced fluid, respectively; $\mathbf{g}$ is the body force (gravity); μ and ν are the dynamic and kinematic viscosities of the fluid; and $\mathbf{x}(t)$ is the location of the center of the particle. This model assumes that the total particle concentration is low, that particle–particle interactions are negligible, and that there is no particle rotation. The terms on the right-hand side of the equation account for buoyancy; pressure gradient; added mass; Stokes drag, including the Faxen correction; and the Basset history integral, which describes the modification of the drag force attributed to the unsteadiness of the flow when a particle accelerates.[25]

To make the Maxey–Riley equation dimensionless and consistent with the hydrodynamic model, the variables were made dimensionless in an analogous way, that is,

$$u_p=\frac{\hat{u}_p}{U_\infty} \qquad v_p=\frac{\hat{v}_p}{U_\infty} \qquad \nu_p=\frac{\hat{\nu}}{aU_\infty} \qquad a_p=\frac{\hat{a}_p}{a} \qquad x=\frac{\hat{x}}{a} \qquad y=\frac{\hat{y}}{a} \quad (8)$$

where u_p, v_p, and t are the dimensionless particle velocities in the x- and y-directions and time, respectively. In this work, the contributions stemming from buoyancy, Faxen correction, and the Basset history integral were neglected because they are considered to be second-order effects. By transforming the variables into dimensionless form, the following 2-D kinematic equations in Cartesian coordinates are obtained for the particles

$$\frac{dx}{dt}=u_p \quad (9)$$

$$\frac{dy}{dt}=\nu_p \quad (10)$$

$$\frac{du_p}{dt}=\left[\frac{1}{(2\gamma+1)}\left(\frac{\partial u}{\partial t}\right)\bigg|_{x=x(t)}+\frac{2}{(2\gamma+1)}\left(\frac{u_p}{2}\right)\left(\frac{\partial u}{\partial x}\right)\bigg|_{x=x(t)}+\frac{2}{(2\gamma+1)}\left(\frac{\nu_p}{2}\right)\left(\frac{\partial u}{\partial y}\right)\bigg|_{x=x(t)}\right]+\left[\frac{2}{(2\gamma+1)}\left(\frac{\partial u}{\partial t}\right)\bigg|_{x=x(t)}+\frac{2}{(2\gamma+1)}(u)\left(\frac{\partial u}{\partial x}\right)\bigg|_{x=x(t)}+\frac{2}{(2\gamma+1)}(\nu)\left(\frac{\partial u}{\partial y}\right)\bigg|_{x=x(t)}\right]+\mathrm{St}(u-u_p) \quad (11)$$

$$\frac{d\nu_p}{dt}=\left[\frac{1}{(2\gamma+1)}\left(\frac{\partial \nu}{\partial t}\right)\bigg|_{x=x(t)}+\frac{2}{(2\gamma+1)}\left(\frac{\nu_p}{2}\right)\left(\frac{\partial \nu}{\partial y}\right)\bigg|_{x=x(t)}+\frac{2}{(2\gamma+1)}\left(\frac{u_p}{2}\right)\left(\frac{\partial \nu}{\partial x}\right)\bigg|_{x=x(t)}\right]+\left[\frac{2}{(2\gamma+1)}\left(\frac{\partial \nu}{\partial t}\right)\bigg|_{x=x(t)}+\frac{2}{(2\gamma+1)}(\nu)\left(\frac{\partial \nu}{\partial y}\right)\bigg|_{x=x(t)}+\frac{2}{(2\gamma+1)}(u)\left(\frac{\partial \nu}{\partial x}\right)\bigg|_{x=x(t)}\right]+\mathrm{St}(\nu-\nu_p) \quad (12)$$

The terms on the righthand side of Eqs. 11 and 12 correspond to contributions arising from added mass (Term 1), the pressure gradient (Term 2), and Stokes drag (Term 3). St is the Stokes number, defined as

$$\mathrm{St}=\frac{2a_P^2\rho_p/\rho}{9\nu}\frac{U}{L}=\frac{2\rho_p/\rho_f}{9}\left(\frac{a_p}{a}\right)^2\mathrm{Re} \quad (13)$$

where ν is the kinematic slurry viscosity, a_p is the particle radius and ρ_p and ρ_f are the densities of the particle and the displaced fluid, respectively. According to this definition of the Stokes number, the Stokes number increases as the particle size increases, and for particles of the same size, the Stokes number increases with increasing particle mass.

Numerical Implementation

The model equations, Eqs. 2–12, were solved using the Euler–Lagrange approach. Spatial derivatives in the mass and momentum balances were discretized on a staggered grid using second-order finite differences in the Navier–Stokes (NSE) and continuity (CE) equations, and a finite-volume discretization in the mass balances to ensure mass conservation.[26] The chosen grid in elliptical coordinates was nonuniform, with a 100×100 resolution, which was sufficient to give grid-independent solutions of the hydrodynamics.[4] Upon spatial discretization the set of differential–algebraic equations (DAE) was time-integrated using LIMEX.[27,28] This solver is based on the extrapolation of a semi-implicit Euler discretization. Special care was taken to ensure consistency in the initial conditions. This was achieved by slowly ramping up the dimensionless inflow velocity from zero to one, while monitoring the residuals of the algebraic subset of the DAE system. The relative tolerance for the time integration was 5×10^{-5}.

The resulting flow field was then interpolated on a Cartesian grid using bicubic interpolation for further use in the particle tracking equations. The Cartesian grid was nonuniform, as shown in Figure 1, for an elliptical bubble with an aspect ratio of $\delta = 0.5$. A coarse grid was used at a distance far from the bubble, where the velocity gradients are constant. Close to the bubble the coarse grid was refined by a factor of 10 in both the x- and y-directions. This provided a very fine grid right near the bubble surface, leading to a better approximation of the curvature of the bubble. During the solution of the particle-tracking equations, the fluid velocity at the particle location is determined by performing a 2-D interpolation of the fluid velocity located at each grid vertex. Because the boundary condition at the bubble surface was that of perfect slip, the 2D interpolation at the bubble surface produced erroneous results arising from zero velocities inside the bubble surface. This was corrected by using a slightly larger bubble than the actual bubble, as shown in Figure 2. The outer bubble was slightly larger (1.7% of the major axis) than the actual bubble surface, which ensured that the 2-D interpolation of the fluid velocities was always completed without incorporating a grid block located inside the actual bubble surface. The effect of this approximation was minimal, given that the radial gradient of the tangential flow component is small, and the radial velocity is set to zero upon collision as described below. The particle-tracking equations were solved using LIMEX with a relative tolerance of 10^{-6}.

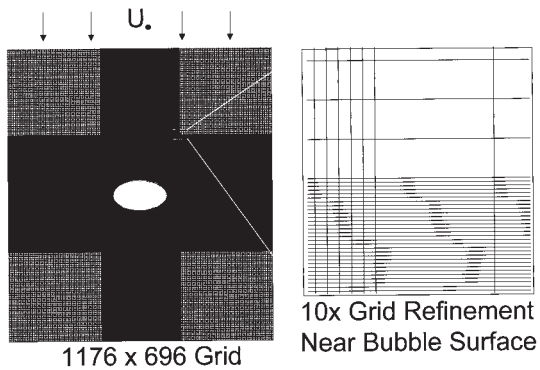

Figure 1. Nonuniform Cartesian grid used in the simulations.

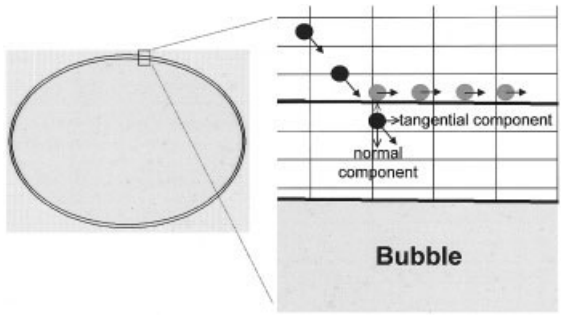

Figure 2. Particle colliding with bubble surface.

The approaching particle is shown in black. After the particle was found inside the outer bubble surface, the particle was moved a distance of 10^{-3} from the bubble surface (shown in gray) and assigned a velocity equal to its tangential component before impact.

In the simulations it was observed that for the higher Stokes numbers, the particles collided with the rising bubble because of their inertia. If a particle collides with the rising bubble, it can either bounce back from the bubble, stay at the interface, or penetrate the bubble.[5] Because our model does not account for particle penetration or particle adhesion, particles have to be transported with the flow around the bubble. Several options were explored to enforce this scenario. In each case, particles that collided with the bubble were moved a distance of $10^{-3} \times d_1$ back from the bubble surface, and were then assigned values for their velocities in both coordinate directions, according to

$$u^o_{p,t} = u_{f,t} \qquad \text{and} \qquad u^o_{p,n} = u_{f,n} \tag{14}$$

$$u^o_{p,t} = \beta \cdot u^i_{p,t} \qquad \text{and} \qquad u^o_{p,n} = \alpha \cdot u^i_{p,n} \tag{15}$$

In Eqs. 14 and 15 the indices p and f denote the particle and the fluid, respectively; i and o denote the velocity of the particle before and after collision with the bubble; t and n denote tangential and normal velocity components with respect to the bubble surface; and α and β specify the collision model. The particles were either assigned the fluid velocity in both coordinate directions (Eq. 14), zero velocity in both coordinate directions ($\beta = \alpha = 0$; Eq. 15), or the tangential velocity of the particle at the time of impact with the bubble surface ($\beta = 1$, $\alpha = 0$; Eq. 15). Although all three scenarios resulted in similar qualitative patterns for particle accumulation, the last model was used for the simulations. In studies on particle–particle interactions, it is often assumed that particles will lose some fraction of their normal velocities and will retain some fraction, β, of their tangential velocity. For the particle–bubble collision, we used a β value of 1 and assumed the particle retains all of its motion in the tangential direction, but loses all motion in the normal direction, as shown in Figure 2.

It was observed that high Stokes number particles eventually gained speed and recollided with the bubble surface after a short distance. Thus, the particles constantly recollided with the bubble surface and moved around the bubble very slowly, resulting in an unusually high particle concentration at the front side of the bubble. This was deemed unrealistic, given that at

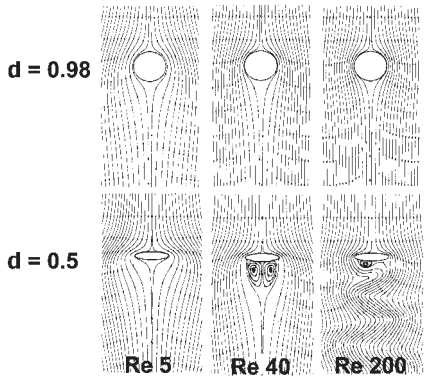

Figure 3. Fluid streamlines around a rising bubble.

The fluid is flowing in the downward direction.

the bubble the fluid flow direction should be exactly tangent to the bubble surface. Therefore, when a particle was found in a grid block that either contained the bubble surface or was adjacent to the bubble surface, the value for the fluid velocity in the Maxey–Riley equations was set equal to the tangential component of the fluid velocity. This kept the particle from continuously recolliding with the bubble surface and reduced the particle concentration in this region.

The results presented in the next section are for a bubble rising in a uniform slurry of catalyst particles. In a first set of simulations, the distribution of particles around a circular bubble was determined for bubble Reynolds numbers of 5, 40, and 200. For circular bubbles (aspect ratio $\delta = 0.98$[1]), there is not enough vorticity generated at the surface of the bubble to cause recirculation or vortex shedding, regardless of Reynolds number. The second case examined the distribution of particles around an elliptical bubble (aspect ratio $\delta = 0.5$). Below a bubble Reynolds number of about 60, the flow is steady; however, the fluid motion in the wake of the bubble is strongly dependent on the bubble Reynolds number. Simulations were performed for bubble Reynolds numbers of 1, 5, 10, 20, 30, and 40. For these cases (both circular and elliptical), 6400 particles were released in the undisturbed flow field far from the bubble surface ($\sim$18 bubble diameters) at a velocity equal to the local fluid velocity; that is, the particles are at rest with respect to the fluid. In the third set of simulations, the unsteady flow around an elliptical bubble ($\delta = 0.5$) was studied for bubble Reynolds numbers of 100 and 200. For these Reynolds numbers, vortex shedding is obtained and the flow is periodic with time, where one vortex is shed from each side of the rising bubble during a single period. For Re 100, one period of flow was divided into 14 equal time snapshots, and 3200 particles (evenly spaced around the centerline) were released at the onset of each snapshot for a total of 44,800 particles. For Re 200, the period was divided into 17 equal snapshots resulting in a total of 54,400 particles tracked around the bubble. In both cases, to ensure accuracy and to account for the time dependency of the flow, the flow between two consecutive snapshots was divided into 100 equal substeps using a linear interpolation. The particles were tracked using the substeps to account for the time-dependent flow.

[1] An aspect ratio of $\delta = 1$ would lead to a singular grid in elliptical coordinates. Thus, a value close to 1 was chosen.

In each of the above-mentioned cases, the particle trajectories within the computational domain were determined by solving Eqs. 9–12. A study was performed to assess how much the individual terms (added mass, pressure gradient, and Stokes drag) contributed to the particle motion. For the closed wake and recirculating fluid cases (Re 1–40), the contributions for a given term were consistent for a given Stokes number. For the lightest particles (St 0.01), the Stokes drag accounted for about 67% of the particle motion, whereas the contribution arising from the pressure gradient was about 22%. For intermediate Stokes numbers, the Stokes drag accounted for 48% of the particle motion, and the contribution stemming from the pressure gradient increased to about 34%. Based on these results, it was decided to account for the contributions arising from added mass, pressure gradient, and Stokes drag.

Catalyst Concentration in the Vicinity of the Bubble

In Figure 3, a few streamlines of the fluid are shown around a rising bubble with aspect ratios of $\delta = 0.98$ and $\delta = 0.5$, respectively, for Re 5, 40, and 200. In this figure, the bubble is rising and the fluid is flowing downward. For the circular bubble the flow is steady and no recirculation or vortex shedding is observed, regardless of the Reynolds number. However, for the elliptical bubble, as the Reynolds number is increased from 5 to 40, a recirculation region develops in the wake of the bubble. The recirculation zone appears at a Reynolds number of about 10, and its size increases with the Reynolds number. As the Reynolds number is increased $>$60, the flow becomes unsteady with respect to time. As shown for a Reynolds number of 200, during one period of flow a vortex is shed from each side of the bubble (that is, two vortices per period). Each vortex is convected downstream from the bubble. The corresponding time-periodic mixing patterns greatly enhance mixing in the bubble wake.

The first set of simulations focused on identifying the particle dispersion as a bubble rises into a uniformly distributed catalyst slurry. Figures 4 and 5 show snapshots of a circular bubble rising into a slurry of catalyst particles with a constant Stokes number for Reynolds numbers of 5 and 200, respectively. The dispersion of 120 particles (out of 6400) is shown at different time steps as the bubble rises into the catalyst slurry. The top row in each set represents particles with a

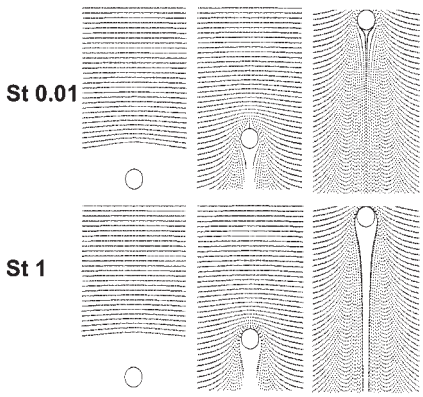

Figure 4. Particle dispersion around a rising bubble ($\delta = 0.98$) with Re 5.

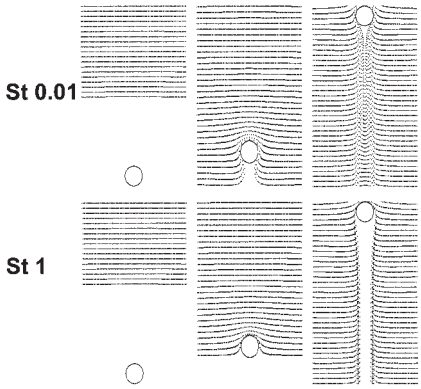

Figure 5. Particle dispersion around a rising bubble (δ = 0.98) with Re 200.

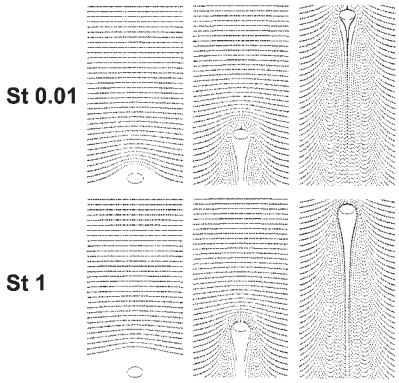

Figure 7. Particle dispersion around a rising bubble (δ = 0.5) with Re 5.

Stokes number of 0.01 (small particles). The bottom rows in each figure represent particles with a Stokes number of 1 (large particles). In each case, the small particles follow the fluid trajectories and show dispersion patterns similar to that of the fluid. However, the large (St = 1) particles are carried by their inertia away from the bubble wake and a significant *particle-free* region develops behind the rising bubbles, which is more pronounced as the Reynolds number increases. Notably, this particle-devoid region is the region that contains the highest dissolved gas concentration, which illustrates the impact of the Stokes number on reaction selectivity: in the case of St = 1 particles, there is significant segregation between gas and catalyst, whereas for the low-Stokes number particles the reaction occurs at high dissolved gas concentrations. This is illustrated in Figure 6, which shows both the H_2 and catalyst concentration behind a bubble for Re = 200 and St = 0.01 and 1. No reaction is occurring in Figure 6. If, say, the undesired reaction had a higher order with respect to hydrogen, the smaller Stokes number (but otherwise identical) catalyst would lead to reduced selectivity and increased by-product formation. Figures 7, 8, and 9 show snapshots of the particle dispersion for an elliptical bubble (δ = 0.5) for bubble Reynolds numbers of Re 5, 40, and 200, that is, for a closed wake, recirculation, and vortex shedding. In all of these figures, the top (bottom) row corresponds to particles with a Stokes number of 0.01 (1.0). As can be seen, the small particles again follow the fluid streamlines, whereas the higher Stokes number particles leave the bubble wake due to their inertia. In the case of Re = 40, however (Figure 8), the primary wake is essentially particle free for both low- and high-Stokes number particles, given that the recirculation and the resulting centrifugal forces do not allow particles to enter the wake in either case. Particles can be found in the recirculation zone only if they were initially present (entered at the injection point) or were transported into the bubble wake by phenomena not accounted for in this study (bubble collision or breakup). However, they are quickly removed from the wake at a rate depending on their Stokes number.[6]

Figure 9 shows the particle distribution as a bubble with Re 200 rises into a slurry of catalyst for St 0.01 and St 1. For the smallest particles, the particles leave a small particle-free region right behind the bubble corresponding to the stable liquid layer, which remains with the rising bubble. The smallest Stokes number particles emulate the fluid trajectories and respond to the changes in fluid direction. The particles move both toward and away from the bubble and can get caught up in loops as the bubble rises. In Figure 10 a few typical trajectories of catalyst particles in the bubble wake, both for St = 0.01 and 1, are shown. It can be seen that some of the trajectories are quite intricate and many of the small particles stay in the bubble wake for an extended period of time. This phenomenon, which is attributed to chaotic Lagrangian mixing in the periodic vortex-shedding flow, was investigated by Koynov and Khi-

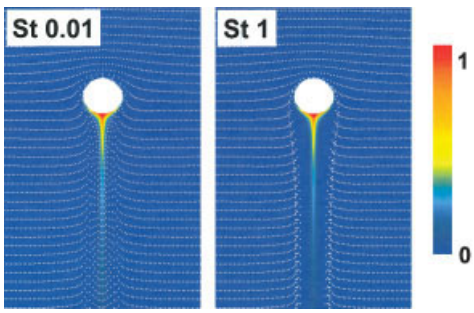

Figure 6. Dissolved gas concentration and normalized particle concentration (δ = 0.98) with Re 200.

Equilibrium concentration of the gas is 1.0. [Color figure can be viewed in the online issue, which is available at www.interscience.wiley.com.]

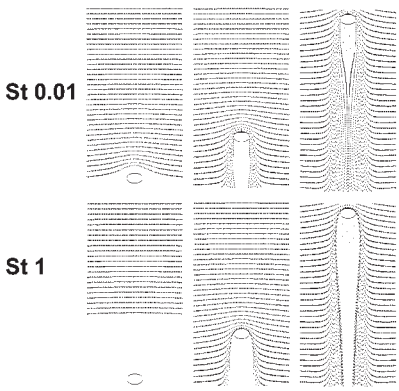

Figure 8. Particle dispersion around a rising bubble (δ = 0.5) with Re 40.

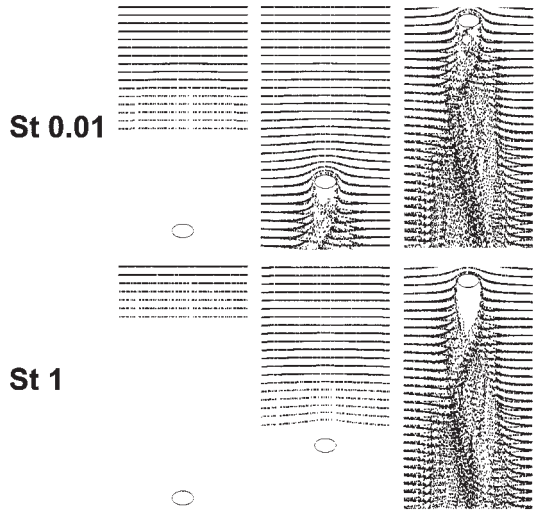

Figure 9. Particle dispersion around a rising bubble (δ = 0.5) with Re 200.

nast[29] and leads to a uniform distribution of particles outside the bubble wake with a slightly higher concentration in the bubble wake (Figure 9). The large particles, however, leave a significant void in the immediate vicinity behind the bubble, but unlike the closed wake cases, they reenter the wake and do not create an extending particle-free wake zone. These plots indicate that particles of St = 1 are slow to respond to the constantly changing fluid patterns, illustrating that particle inertia is a dominant contributor to the motion of a particle.

Based on the trajectories of the particles, spatially and time-averaged catalyst concentration fields were generated that show the average slurry concentration relative to the undisturbed uniform slurry, as shown in Figure 11 for an elliptical bubble with vortex shedding (Re = 100) and for large particles (St = 1). To generate these plots, a uniform grid was placed over the computational domain. As the particles moved across the domain, the number of particle hits per grid block was counted and, then, each grid block was divided by the number of hits in

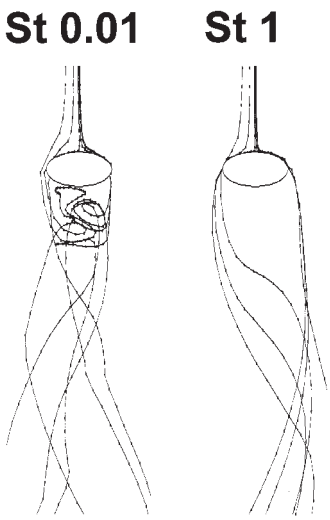

Figure 10. Particle trajectories around a rising bubble (δ = 0.5) with Re 200.

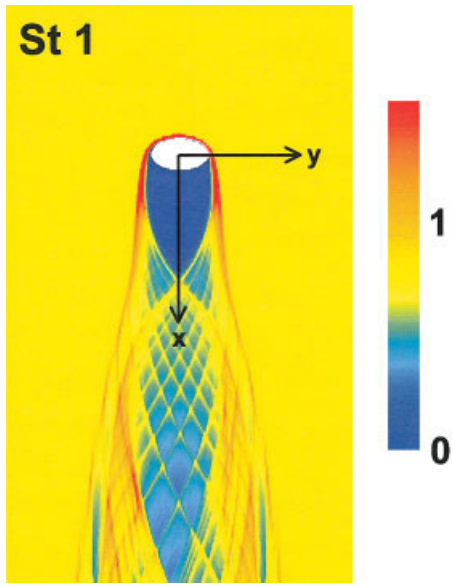

Figure 11. Normalized particle concentration around the bubble (δ = 0.5) with Re 100.

[Color figure can be viewed in the online issue, which is available at www.interscience.wiley.com.]

the undisturbed flow field at the top center of each domain to normalize the plots. Thus, the spatial averaging occurs on a scale similar to the grid size. In Figure 11, yellow represents a normalized value of one (that is, the concentration of the undisturbed slurry) and red shows regions of high catalyst concentration. As can be seen, the concentration of catalyst particles close to the bubble roof is high because catalyst particles collide with the bubble (St = 1) and slowly accelerate with the bubble. Thus, not only particles in the bubble wake have to be accelerated, but also particles at the roof (which has to be accounted for in the "added mass" term in Euler–Lagrange simulations of bubbles rising in slurries). In addition, in the bubble wake an intricate pattern of streaks can be observed. In our computations we tried to establish whether these streaks are numerical artifacts by changing the resolution, the averaging procedure, and other numerical parameters. However, the streaks were robust features of the simulations and did not vanish. Thus, these patterns might be the result of the chaotic mixing in the bubble wake in the case of time-periodic vortex shedding. Further studies will aim at elucidating this feature.

The spatially and time-averaged plots were computed for each case and further analyzed by computing statistical averages of the catalyst concentration. For example, the dispersion function $D_y^2(x)$, as given by Chein and Chung,[18] is

$$D_y^2(x) = \frac{1}{N_y} \sum_{j=1}^{N_y} [Y_j(x) - Y_{avg}(x)]^2 \tag{16}$$

where N_y is the total number of grid points perpendicular to the flow directions, and $Y_j(x)$ denotes the local normalized slurry concentration (Y_j = 1 corresponds to uniform slurry) as a function of x (that is, dimensionless distance from the bubble center as shown in Figure 11). The average catalyst concentration at position $Y_{avg}(x)$ is

$$Y_{avg}(x) = \frac{1}{N_y}\sum_{j=1}^{N_y} Y_j(x) \tag{17}$$

Clearly, the function in Eq. 16 depends on the number of grid cells and the width of the domain [that is, for $y \to \infty : D_y^2(x) \to 0$]. We limited the domain to $-8 < y < 8$, where y is the distance perpendicular to the flow made dimensionless by d_1.

Figure 12 shows the particle dispersion plots for Re 5, 40, and 200 for a bubble with aspect ratio $\delta = 0.98$ at St 0.01 and 1. In this figure, the particle dispersion function is plotted against the downstream distance x. To achieve smoother functions, 10 grid blocks were averaged in the x-direction, which did not change the quality of the plot, but reduced the variations that are introduced by using a finite number of particles for the generation of the catalyst density plots. In Figure 12, a value of zero on the particle dispersion axis represents a uniform distribution of particles perpendicular to the flow; that is, no particles are removed from the wake. As can be seen in all of these plots, the lowest Stokes number particles show the least amount of dispersion, as expected. For Re = 5 in both cases (St = 0.01 and 1) the dispersion is initially high because the bubble "splits" the flow. However at St = 1, the dispersion function at $x = 0$ is higher than that at St 0.01. This change in dispersion is explained by the higher concentration of particles at the bubble surface, given that, as described above, large particles collide with the bubble and are accelerated (with respect to the fluid) by the bubble, whereas small particles flow around the bubble and do not stay at the surface. In the case of the small particles, the dispersion decreases with the distance from the bubble as the particles follow the flow. In contrast, the larger particles remain on their trajectory and do not reenter the wake region once they have passed the bubble. We also performed simulations for St = 0.1 (not shown) and the St = 0.1 particles behaved approximately in the same way as the St = 0.01 particles.

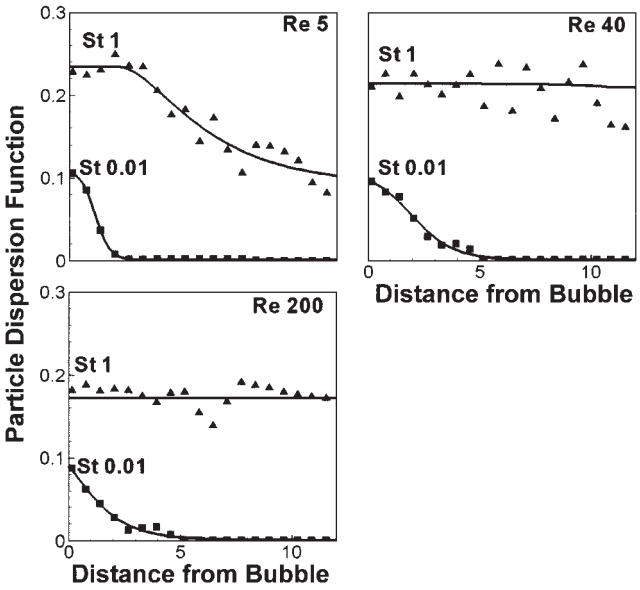

Figure 12. Particle dispersion in the wake of a bubble ($\delta = 0.98$) for Re 5, 40, and 200.

Lines are drawn to aid the eye.

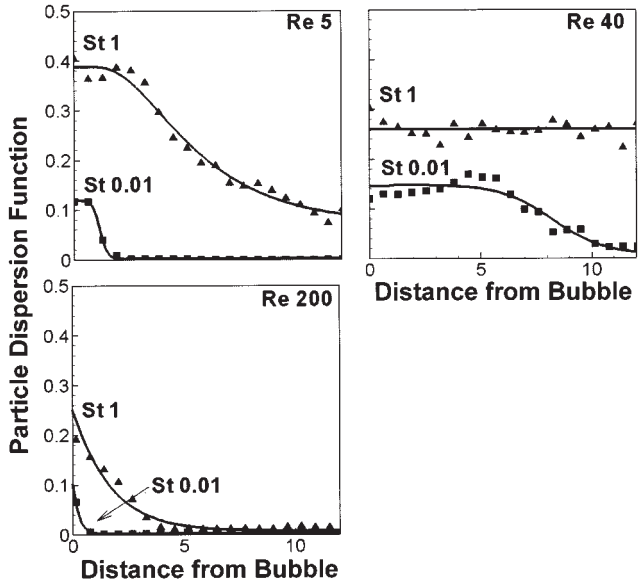

Figure 13. Particle dispersion in the wake of a rising bubble ($\delta = 0.5$) for Re 5, 40, and 200.

Lines are drawn to aid the eye.

Figure 13 shows the particle dispersion for the elliptical bubble at three different Reynolds numbers (Re = 5, 40, 200) and St = 0.01 and 1. At Re = 5, the flow has a closed wake pattern with no recirculation present. The dispersion functions for both St numbers are similar to those for the circular bubble. For Re = 40, a large recirculation zone forms in the bubble's wake, and as the bubble rises into a slurry, the particles do not enter the recirculation zone (see Figure 8). In the dispersion plots this behavior is reflected by the high dispersion function behind the bubble for both St = 0.01 and St = 1. However, once the light particles are transported past the recirculation zone, they follow the streamlines (see Figure 3) and move into the wake, which is reflected by the decrease in dispersion. Finally, Figure 13 shows the particle dispersion for the vortex-shedding case of Re = 200. The smallest particles do not show any significant dispersion. On the contrary, the concentration of particles in the primary wake of the bubble is even slightly higher than that in the rest of the wake. For the heavy particles there is a small region behind the bubble, which is particle free. However, particles are quickly entering the wake region, leading to a reduction of the dispersion function.

We also computed the average dispersion function $D_{avg}^2(y)$ for a given Reynolds and Stokes number, which is a characteristic of the cumulative particle dispersions caused by one bubble. For this case we averaged the particle density over both the x- and y-directions, as follows

$$D_{avg}^2 = \frac{1}{N_x}\sum_{i}^{N_x} D_y^2(x) \tag{18}$$

where N_x is the total number of grid points in the x-direction. Figures 14 and 15 show the average particle dispersion vs. the

Reynolds number for circular and elliptical bubbles, respectively. Unlike the previous plots that show the particle dispersion as a function of distance from the bubble, the average particle dispersion was calculated over the entire grid domain. As shown in Figure 14, the average particle dispersion for a circular bubble is small and almost constant in the case of St = 0.01 and 0.1, that is, the particles that are small and intermediate in size. However, the dispersion in the case of the large particles (St = 1) is significantly increased and is the largest for low Reynolds numbers, as the particles accumulate close to the bubbles roof. As the Reynolds number increases, these particles are quickly swept away by the flow, reducing the average dispersions. For elliptical bubbles (Figure 15), the situation is fundamentally different because there exists a maximum at intermediate Reynolds numbers that results from the recirculation zone behind the bubble. Vortex shedding causes an increase in transport back in the wake, leading to a smaller average dispersion.

A catalyzed chemical reaction occurs when both gas and catalyst are present at the same location. Given that particles are discrete objects, a continuum hypothesis has to be invoked that allows us to treat the catalyst as a continuous phase. Catalyst particles in a slurry are usually small (between 1 and 100 μm). Assuming an average particle size of 30 μm and a catalyst loading of 5 vol %, the maximum distance a liquid molecule has to travel to reach the surface of a catalyst particle is on the order of 50 μm. Thus, at elevated temperatures, the distribution of the catalyst can be viewed as a continuum, and the local reaction rate is a function of the local catalyst concentration computed by the averaging process described above. Invoking the continuum hypothesis for the catalyst, a cross-correlation coefficient (*CCC*) can be defined that determines the correlation of particles and dissolved gas. A high *CCC* value relates to a system where both the gas and the catalyst have high concentrations at the same location, whereas a low *CCC* value indicates significant segregation (that is, gas and catalyst are present at different locations). Figure 16 shows the local correlation coefficient C_{local}

$$C_{local} = \frac{c_{gas} \cdot c_{cat}}{c_{gas,avg} \cdot c_{cat,slurry}} \tag{19}$$

where $c_{gas,avg}$ is the average gas concentration in kmol/m^3 for given Reynolds and Schmidt numbers, and $c_{cat,slurry}$ is the

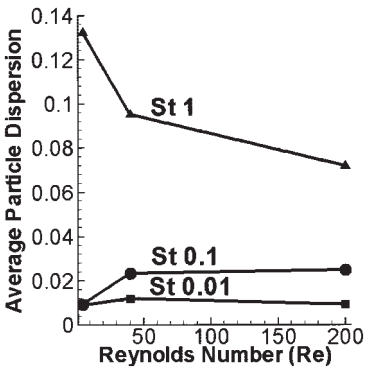

Figure 14. Average particle dispersion vs. Reynolds number (δ = 0.98).

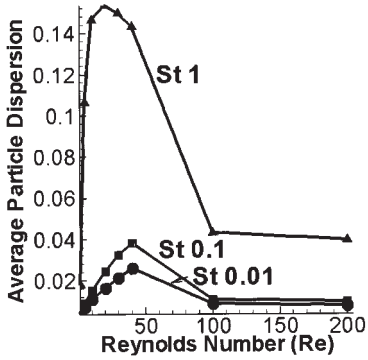

Figure 15. Average particle dispersion vs. Reynolds number (δ = 0.5).

catalyst concentration in kg/m^3 for the undisturbed slurry. From Figure 16, it can be seen that, depending on the flow, the local cross-correlation is very different. In the case of Re = 5 and St = 0.01, C_{local} is high everywhere in the wake, except for the direct fluid layer adjacent to the bubble base. For higher Reynolds numbers (Re = 40), C_{local} is essentially zero in the primary wake, whereas in the vortex-shedding case (Re = 200), the local correlation is only high directly in the wake. Finally, in Figure 17 the integral cross-correlation coefficient for elliptical bubbles is reported, which is defined as

$$CCC = \frac{1}{\tau A}\int\int\int C_{local}(t)dxdydt. \tag{20}$$

In the case of unsteady vortex shedding, the instantaneous local cross-correlation was integrated over one period of vortex shedding τ. In Figure 17, the correlation coefficient is plotted against the Reynolds number for Stokes numbers of 0.01 and 1.0. For a given Stokes number, the *CCC* is smallest when recirculation is present in the wake (Re 10–50) and increases in the vortex-shedding regime. The maximum *CCC* values are obtained for the closed wake fluid cases (Re < 10). Additionally, the higher the Stokes number, the lower the cross-correlation, given that inertia tends to separate the catalyst from regions with high dissolved gas concentrations. The Schmidt number (ν/D) is varied in these plots. Thus, Figure 17 presents a universal plot that indicates how well gas and catalyst "mix." As shown in this figure, the trends for the cross-correlation coefficient are similar regardless of Schmidt number. However, as the Schmidt number decreases, the *CCC* value increases for a given Reynolds and Stokes number as the diffusivity at constant viscosity increases. The impact on the St = 0.01 particles is relatively small because the small particles typically enter the wake, where the gas concentration is highest, regardless of the Schmidt number. The plot in Figure 17 also can be used to predict the selectivity of reactions. For example, if the desired reaction has higher order with respect to the gas concentration than the undesired reaction (that is, the selectivity is proportional to the dissolved gas concentration) the optimal case is a high cross-correlation coefficient because the reaction will occur at higher levels of the dissolved gas. In this fashion, the charts in Figure 17 can then be used as a predictive tool to maximize the yield and selectivity for a given reaction system.

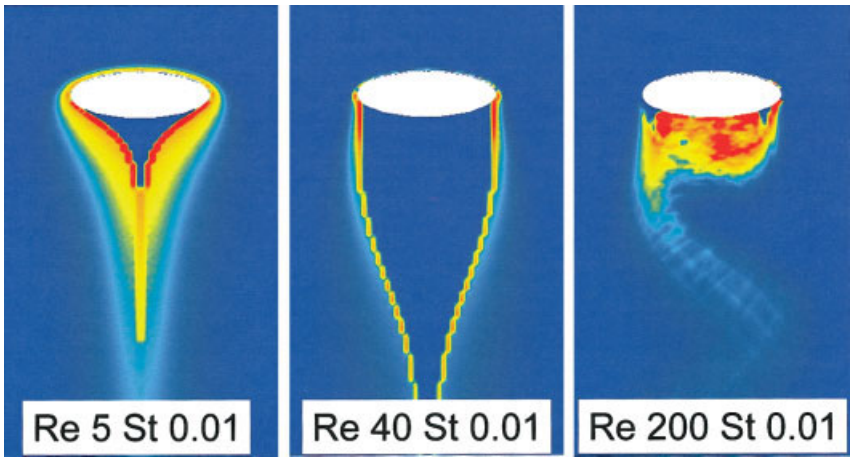

Figure 16. Correlation between dissolved gas (Sc 40) and particles around a rising bubble (δ = 0.5).

[Color figure can be viewed in the online issue, which is available at www.interscience.wiley.com.]

In the case of unsteady wakes the gas and the catalyst concentration fluctuates. It is well known that the fluctuations will have an impact on the reaction rate and selectivity. For example, if the rate of the desired reaction is proportional to $c_{cat} \cdot c_{gas}$, then the averaged rate is not proportional to $\overline{c_{gas}} \cdot \overline{c_{cat}}$ because $\overline{c_{gas} \cdot c_{cat}} \neq \overline{c_{gas}} \cdot \overline{c_{cat}}$. In Figure 18, the fluctuations of the catalyst particle concentration over dimensionless time are shown for a "test zone" in the wake of the bubble (x = 5, y = 0) and for two Reynolds numbers (Re = 100 and 200). The test zone is located downstream of the bubble surface and is off center. It can be seen that in both cases there are significant fluctuations. In the case of Re = 100, the amplitudes are large, whereas in the case of Re = 200 the amplitudes are much smaller, in that at this Reynolds number the catalyst particles are constantly transported out of the wake. The corresponding concentration of hydrogen at the same location is shown in Figure 19 for Schmidt numbers of 40 and 160. In both cases, periodic fluctuations occur, where one peak is higher than the other (in the case of Re = 100 the difference is very small) attributed to the off-center location of the test zone. Because the gas concentration in the vortices is relatively high, the peak has a higher amplitude, when a vortex passes through the test zone. For Re = 100, St 0.01, and Sc = 160, the $\overline{c_{gas} \cdot c_{cat}}$ = 0.016 and $\overline{c_{gas} \cdot c_{cat}}$ = 0.020. Thus, it can be seen that it is important to include the microscale fluctuations of both catalyst and gas in the analysis.

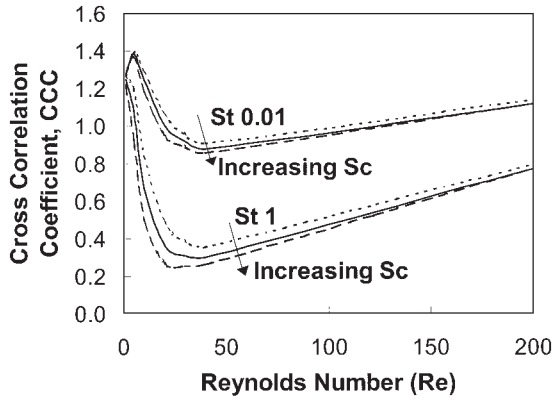

Figure 17. Cross-correlation coefficient vs. Stokes number for a rising bubble (δ = 0.5) for Sc = 40, 80, and 160.

Impact of Catalyst Distribution on By-Product Formation

In this section, two different industrially relevant parallel–consecutive reaction networks will be studied to illustrate how the bubble and particle properties can influence the selectivity of a specific reaction network (Eqs. 21 and 22). The parallel reaction networks shown in Eqs. 21 and 22 were chosen to demonstrate the impact of particle concentration on reaction selectivity. A is the liquid phase reactant, G represents the dissolved gas, P is the desired product, and U is the undesired product. In both reactions, the desired reaction is catalyzed,

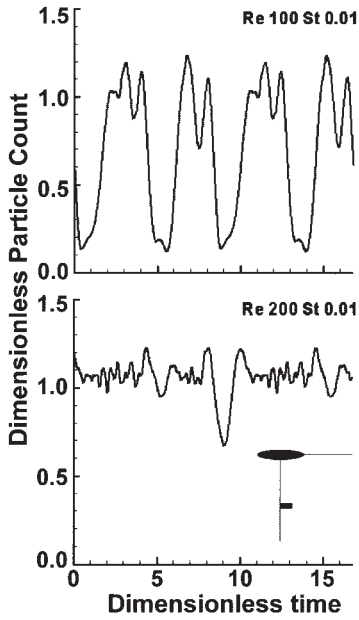

Figure 18. Particle fluctuations in the wake of a rising bubble (δ = 0.5) in the vortex-shedding regime (Re 100 and 200).

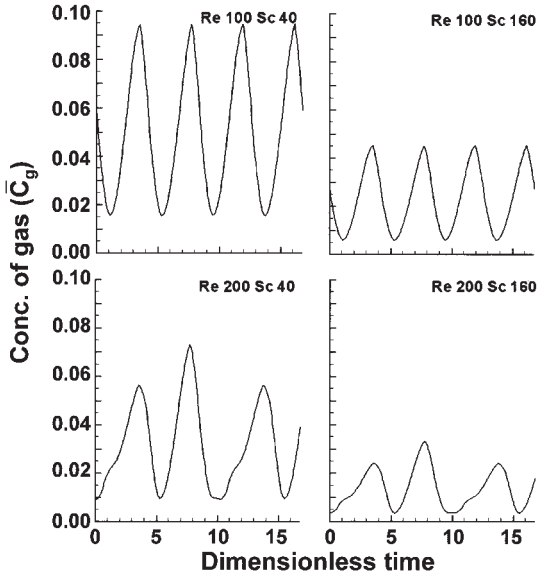

Figure 19. Gas fluctuations in the wake of a rising bubble (δ = 0.5) for Re 100 and 200.

whereas the undesired side reaction is slower and not catalyzed.

$$A + G \xrightarrow{cat} P \qquad r_1 = \mathrm{Da}_1 c_G c_A c_{cat}$$

$$A + P \rightarrow U \qquad r_2 = \mathrm{Da}_2 c_P c_A \tag{21}$$

$$A + G \xrightarrow{cat} r_1 = \mathrm{Da}_1 c_G c_A c_{cat}$$

$$G + P \rightarrow U \qquad r_2 = \mathrm{Da}_2 c_P c_G \tag{22}$$

where Da_1 and Da_2 are the Damköhler numbers for reactions 1 and 2, respectively. The scalar transport equations for the reactive species in dimensionless form are

$$\frac{\partial c_i}{\partial t} + \frac{1}{h}\left(u\frac{\partial c_i}{\partial \eta} + \nu\frac{\partial c_i}{\partial \varphi}\right) = \frac{1}{\mathrm{Pe}_i h^2}\left(\frac{\partial^2 c_i}{\partial \eta^2} + \frac{\partial^2 c_i}{\partial \varphi^2}\right) + \sum_{j=1}^{m} \nu_{ij} r_j(c_i) \qquad i = A, G, P, U; j = 1, 2 \tag{23}$$

In Eq. 23 the concentrations are made dimensionless by dividing each concentration by $c_{A,\mathrm{in}}$ at the inflow, that is, the bulk concentration of the liquid-phase reactant. The Peclet number of every component is $\mathrm{Pe}_i = U_\infty a/D_i = \mathrm{Re}\cdot\mathrm{Sc}_i$, where Sc_i is the Schmidt number of species i. The boundary conditions at the bubble surface are those of zero flux for P and U, and the concentration of the gaseous reactant at the bubble surface is assumed to be equal to the dimensionless equilibrium concentration c_G^*.

In both reaction networks, the desired reaction occurs only in the presence of a catalyst. The dimensionless catalyst concentration is c_{cat}, where $c_{cat} = c_{cat,local}/c_{cat,slurry}$, and was computed using the particle-tracking simulations described above. $c_{cat,local}$ is the local catalyst loading in kg/m^3. It is assumed that the undesired reaction is noncatalytic.

By using the cross-correlation diagram in Figure 17, we can preselect the conditions that should favor the desired reaction. For example, the reaction rate of the desired reaction will be favored by a high cross-correlation coefficient *CCC* (as only the desired reaction is catalyzed in both cases). Consequently, it may be expected that the selectivity is high if the *CCC* is large. Thus, the diagram in Figure 17 suggests that St 0.01 particles, instead of the St 0.1 and St 1 particles, should give a higher selectivity, regardless of the Reynolds number. In addition, for given Stokes and Reynolds numbers, the *CCC* increases with decreasing Schmidt numbers. For a given Schmidt number and Stokes number, the cross-correlation value is highest for the closed wake fluid regimes (Re $<$ 10). For the larger particles (St = 1), the *CCC* is higher for the vortex-shedding cases (Re $>$ 60) than that for the recirculating wake cases (10 $<$ Re $<$ 60), thus indicating that operating at a high Reynolds number should favor the selectivity for the desired reaction compared to intermediate Reynolds numbers. Therefore, because the desired catalyzed reaction is identical for the two example reaction networks, we expect that operating in the closed-wake regime (Re $<$ 10) with the smallest particles (St = 0.01) at the lowest Schmidt number (Sc = 40) will yield the highest selectivity in both cases. In the following section this hypothesis is tested by using numerical simulations of the reactions close to bubbles. The bubble was assumed to contain a pure gas, and thus no depletion effects were considered (equilibrium concentration is constant). The overall selectivity toward the desired product for a given set of conditions was calculated by dividing the total amount of the desired product over the sum of the total products formed within the grid domain, as shown in the following equation

$$S = \left(\frac{P_{tot}}{P_{tot} + U_{tot}}\right) \tag{24}$$

The selectivity for the vortex-shedding cases was time-averaged over one period.

Reaction 1

The first parallel–consecutive reaction network is given by Eq. 21. In this reaction, A (a dilute liquid-phase reactant) reacts with the dissolved gaseous species G in the presence of a catalyst to form the desired product P. Reactants A and P can then react to form the undesired product U. The Damköhler numbers in the reaction rate expressions are given by

$$\mathrm{Da}_1 = \frac{a k_1 c_{A,in} c_{cat,slurry}}{U_\infty} \qquad \mathrm{Da}_2 = \frac{a k_2 c_{A,in} c_{cat,slurry}}{U_\infty} \tag{25}$$

where $c_{A,in}$ is the inflow concentration of reactant A, that is, the bulk concentration of A. The system properties used for the simulations are presented in Table 1.

Examination of the parameters in Table 1 shows that the desired reaction is always faster than the undesired reaction

Table 1. Parameters Used for Reaction 1

Parameter	Value
Da_1	1000
Da_2	50
Sc_G	40
Sc_P, Sc_U	50
$\hat{c}_G^*$	5.1

when a catalyst is present (effective ratio of $k_1/k_2 = 20$). The undesired reaction, however, will occur anywhere where P and A coexist. Thus, low selectivity will be obtained if A and P have significant concentrations at the same location. In contrast, segregation of the two reactants will lead to high selectivity. To prevent formation of the undesired product, A must become locally depleted. Therefore, if A is in excess of G, the undesired reaction will always occur, reducing the overall selectivity.

The selectivity as a function of the bubble Reynolds number and the particle Stokes number is presented in Figure 20. It can be observed that the selectivity decreases dramatically with the Reynolds number (from 70 to 30%) and also decreases with the particle Stokes number. The highest selectivity can be achieved at Re = 1, regardless of the Stokes number. At Re = 1, the fluid flow is steady and no recirculation is present. The smallest particles, St = 0.01, fill the wake region completely, whereas the intermediate and largest particles (St = 0.1 and St = 1) leave only a very narrow void region behind the rising bubble. Therefore, no impact of the Stokes number is observed. In addition, the gas concentration in the wake is very high (see Khinast[4]), leading to a local depletion of A, which cannot react with P to form U. Furthermore, the residence time of P in the wake is low, so that P is transported away quickly and is quickly diluted, leading to a negligible rate of the side reaction. The selectivity for the recirculating-wake cases, Re = 10, 20, and 40, decreases as the Re and St numbers increase. Because the particles do not enter the recirculation region, the product P is formed outside the recirculation region and diffuses into it, leading to a high concentration (long residence time) in the recirculating wake, as illustrated in Figure 21. As can be seen in these snapshots, the product is formed outside the recirculation region, but is then transported into the recirculation region by diffusion. The highest rate of diffusion of P into the recirculation region occurs near the bottom of the region. While the product is recirculating, it is reacting with A to form the undesired product. The undesired reaction occurs in all areas of the recirculation zone because the concentration of P is high. Because the size of the recirculation region increases as Re increases, the amount of undesired product formed increases with increasing Re number, thus lowering the overall selectivity. For the recirculating-wake cases, the lower St number particles give a higher selectivity for a given Re number, given that these particles tend to follow the closed-wake fluid

Table 2. Parameters Used for Reaction 2

Parameter	Value
Da_1	1000
Da_2	50
Sc_G	40
Sc_P, Sc_U	50
$\hat{c}_G^*$	0.08

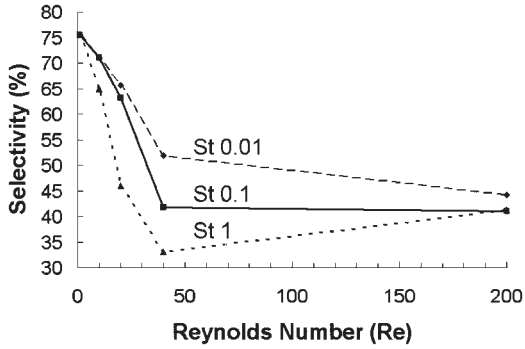

Figure 20. Selectivity as a function of Reynolds and Stokes numbers for a rising elliptical bubble ($\delta = 0.5$) for test reaction 1.

patterns and leave less of a void region than the higher St number particles.

In the case of vortex shedding (Figure 20) the selectivity remains almost constant. This is surprising, in that fluid and dissolved gas are quickly convected downstream, and no stagnation regions exist in the wake. Thus, it should be the optimum conditions for running a reaction of this type. Also the *CCC* values in Figure 17 suggest a recovery of the selectivity. The reason for this phenomenon is that liquid-phase reactant, gas, products, and catalyst are intimately mixed in a large wake region downstream of the bubble. Thus, because there is no segregation, both the desired and undesired reactions will occur over a large area, lowering the selectivity. Therefore, the overall yield is increased, but the selectivity is low in the vortex-shedding regime. It can also be seen for the Re = 200 case that the selectivity is independent of the Stokes number, indicating that the mixing is sufficient for all types of particles.

Inspection of cross-correlation diagrams reveals that in fact this diagram predicts the selectivity dependency on Stokes and Reynolds numbers quite well. The highest selectivities are obtained for the smallest Stokes number particles (St 0.01), regardless of Reynolds number. Operating in the closed-wake fluid regime (Re < 10) also gives higher selectivity than the intermediate or high Reynolds number flows, as predicted by Figure 17.

Reaction 2

The second parallel–consecutive reaction network is given by Eq. 22 and Table 2. In this example, the desired reaction is identical to that in reaction 1. Unlike the first example, however, the product P competes with A by reacting with G to form

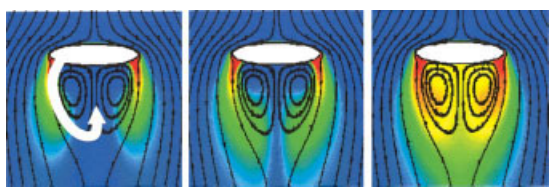

Figure 21. Snapshots of the developing concentration of forming product P in the wake.

[Color figure can be viewed in the online issue, which is available at www.interscience.wiley.com.]

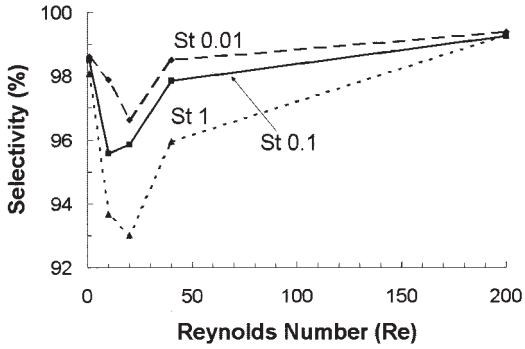

Figure 22. Selectivity as a function of Reynolds and Stokes numbers for a rising elliptical bubble ($\delta = 0.5$) for test reaction 2.

the undesired product *U*. The Damköhler numbers in the reaction rate expressions are the same as in case 1.

Unlike reaction 1, this reaction can be run with excess *A* because it will not promote formation of the undesired product. Furthermore, the undesired reaction will occur only where local concentrations of *P* and *G* coexist. If *A* and catalyst are present, the desired reaction will be favored over the undesired reaction as a result of the reaction rate constants of this system. Therefore, the desired reaction will be favored if *G* is transported out of the wake and into regions rich in both *A* and catalyst particles. The selectivity results for reaction 2 as a function of the bubble Reynolds number and the particle Stokes number are shown in Figure 22. It can be seen that this diagram follows approximately the trend suggested by the cross-correlation diagram from Figure 17. The highest selectivities are achieved for Re = 200 and the second highest selectivities are obtained for conditions when no recirculation occurs in the bubble wake (Re = 1). Clearly, the selectivity decreases with Stokes number. As can be seen from Figure 22, the selectivity for the closed-wake case with no recirculation (Re = 1) is high because both catalyst and gas coexist.

Higher Stokes numbers lead to minimal segregation, thus slightly reducing the selectivity. As soon as recirculation is obtained, the selectivity decreases. As discussed earlier, when a bubble rises into a slurry of catalyst particles, the particles do not enter the steady recirculation region regardless of their St number. Therefore, *P* is produced at the border of the recirculation region, and it diffuses into the recirculation region and/or is convected downstream. The portion that diffuses into the recirculation region reacts with the dissolved gas to form the undesired product, thus lowering the selectivity. Interestingly, it can be seen that the selectivity for the recirculating wake cases decreases as the recirculation region increases in size until it reaches a critical point, at which an increase in the recirculation region size does not further decrease the selectivity, but rather increases it. This can be explained by examining the difference between the rate of diffusion into the zone relative to the rate of (undesired) reaction area in the recirculation zone. As the Reynolds number is increased, the recirculation area increases, its size being approximately proportional to the square of its radius. The area through which diffusion occurs (that is, the circumference) is proportional to the radius. Therefore, the diffusion into the wake becomes less important as the size of the recirculation zone increases, effectively limiting the contribution of the undesired reaction. Thus, at a critical size of the recirculation zone, an increase in the recirculation area results in an increase in reaction selectivity.

The highest selectivities are observed for the vortex-shedding case (Re = 200). Because the gas is quickly convected downstream into regions rich in reactant *A* and catalyst, the desired reaction is promoted, the gas is quickly consumed, and minimal undesired product is formed. The effect of the Stokes number at a given Reynolds number shows similar trends to that observed in reaction 1, given that the void region in the bubble wake is the highest for high Stokes numbers, leading to a segregation of gas and catalyst.

Comparison of these results to those predicted using the cross-correlation diagrams shows their limitations. Although the overall trend is well captured, some differences exist that make direct numerical simulations indispensable. As predicted, the smallest particles result in the highest selectivities, regardless of Reynolds number. Based on the correlation diagrams, we expected the selectivity to decrease with increasing Reynolds number in the recirculation regime, which indeed happens until a critical recirculation size is reached. Above Re = 20, the selectivity increases again. Therefore, the predictive diagrams offer a good starting point for picking reaction conditions but other parameters (such as residence time, diffusion rate, reaction rates) can influence the final results.

Summary and Conclusions

In this work, numerical simulations were performed to show how bubble properties (size and shape) and particle properties (mass and size) can influence the selectivity of fast heterogeneously catalyzed gas–liquid reactions. The dynamics of the bubble wake are dependent on both the bubble shape and the fluid properties (densities, viscosities, surface tension) and can be either time independent (closed wake with or without recirculation) or time dependent (vortex shedding). Elliptical bubbles can exhibit any of these wake types, whereas circular bubbles are limited to the closed wake without recirculation. The Stokes number influences how catalytic particles travel around a rising bubble. The particle trajectories were modeled using the Maxey–Riley equation accounting for contributions stemming from added mass, pressure gradient, and Stokes drag. A statistical analysis was performed to show how the particles distribute in the bubble wake. The main findings of our work are as follows:

- The wake structure determines how well the dissolved gas mixes and where catalyst particles concentrate as a bubble rises through a catalyst slurry. Because the wake structure depends on the bubble shape and Reynolds number, the operating and design parameters of a given system can influence both the mixing and reaction performance of heterogeneously catalyzed fast gas–liquid reactions.
- The Stokes number influences the particle distribution around a rising bubble. Small St number particles tend to follow the fluid patterns, but will not enter recirculation regions. Intermediate and large St number particles do not follow the streamlines and leave large void regions in the wake of a bubble, at the same location, where the gas concentration is highest (segregation).
- Two reaction networks were used to show how the selectivity of fast gas–liquid catalyzed reactions can be significantly

changed by choosing the appropriate operating conditions of a bubble column and the size of catalyst particles. Because even a small decrease in the reaction selectivity can translate into a large increase in production costs (arising from rework, separation, or disposal), it is crucial to understand how the bubble and catalyst properties influence the overall reaction performance. Because most systems are too complicated to understand them on an intuitive basis, numerical simulations are needed to elucidate the complex dependencies of selectivity on the system parameters.

• The methodology developed can be used as a guide for selecting optimal operating conditions for heterogeneously catalyzed fast gas–liquid reactions. The most important information is the cross-correlation coefficient of the dissolved gas concentration and the particle concentration for a given bubble Re number and particle St number.

Future work will address experimental confirmation of our predictions and a more detailed description of the gas–liquid–solid flow.

Acknowledgments

The authors acknowledge support of this work by Merck & Company, NSF Grant CTS 02098764 and ACS Grant 36283-G9.

Notation

a = half the interfocal distance of the ellipse, m
a_p = radius of particle, m
c_i = dimensionless concentration of species i
$\hat{c}_i$ = concentration of species i, kmol/m^3
c^* = equilibrium gas concentration at bubble surface
$c_{cat,slurry}$ = catalyst loading, kg/m^3
Da_1 = Damköhler number of reaction 1
Da_2 = Damköhler number of reaction 2
D_i = diffusion constant in the liquid phase of species i, m^2/s
$d_{1(2)}$ = major (minor) semiaxis of the ellipse, m
$\mathbf{g}$ = gravitational vector, m/s^2
h = dimensionless scale factor
$k_{1,2}$ = reaction rate constants, m^6 kg$_{cat}^{-1}$ kmol^{-1} s^{-1}
L = characteristic length, m
m_f = mass of the displaced fluid, kg
m_p = mass of the particle, kg
N_i = convective and diffusive fluxes, kmol m^{-2} s^{-1}
P = dimensionless pressure
$\hat{P}$ = pressure, Pa
Pe_i = Peclet number of species i, $U_\infty a/D_i$
r = dimensionless reaction rate
$\widehat{Re}$ = Reynolds number based on a, $aU_\infty\rho/\mu$
Re = Reynolds number, $d_1U_\infty\rho/\mu$
Sc_i = Schmidt number of species i, $\nu/(D_i)$
St = Stokes number (see Eq. 13)
$\hat{t}$ = time, s
t = dimensionless time
Δt = dimensionless time step
u = dimensionless velocity in η-direction
u_p = dimensionless particle velocity in η-direction
$\hat{u}$ = velocity in η-direction, m/s
$\hat{u}_p$ = velocity of particle in η-direction, m/s
U = characteristic velocity, m/s
U_∞ = terminal bubble rise velocity, m/s
v = dimensionless velocity in φ-direction
v_p = dimensionless particle velocity in φ-direction
$\hat{v}$ = velocity in φ-direction, m/s
$\hat{v}_p$ = velocity of particle in φ-direction, m/s
x = physical x-coordinate, m
$\mathbf{x}(t)$ = location of center of particle, m
y = physical y-coordinate, m
Y_P = selectivity (see Eq. 15)

Greek letters

δ = aspect ratio d_2/d_1
η = transformed coordinate direction
φ = transformed coordinate direction
μ = liquid viscosity, Pa·s
ρ = liquid density, kg/m^3
ρ_p = density of the particle, kg/m^3
ν = kinematic viscosity, m^2/s

Literature Cited

1. Ramachandran PA, Chaudhari RV. *Three Phase Catalytic Reactors.* New York, NY: Gordon & Breach; 1983.
2. Mills PL, Chaudhari RV. Reaction engineering of emerging oxidation processes. *Catal Today*. 1999;48:17-29.
3. Beenackers AACM, van Swaaij WPM. Mass transfer in gas–liquid slurry reactors. *Chem Eng Sci*. 1993;48:3109-3139.
4. Khinast JG. Impact of 2-D bubble dynamics on the selectivity of fast gas–liquid reactions. *AIChE J*. 2001;47:2304-2319.
5. Fan LS, Tsuchiya K. *Bubble Wake Dynamics in Liquids and Liquid–Solid Suspensions.* Boston, MA: Butterworth-Heinemann; 1990.
6. Raffensberger JA, Koynov AA, Glasser BJ, Khinast JG. Influence of particle properties on the yield and selectivity of fast heterogeneously catalyzed gas–liquid reactions. *Int J Chem React Eng*. 2003;1:A15.
7. Khinast JG, Koynov A, Leib TM. Reactive mass transfer at gas–liquid interfaces: Impact of micro-scale fluid dynamics on yield and selectivity of liquid-phase cyclohexane oxidation. *Chem Eng Sci*. 2003;58:3961-3971.
8. Paul EL, Treybal R. Mixing and product distribution for a liquid-phase, second-order, competitive consecutive reaction. *AIChE J*. 1971;17:718-724.
9. Baldyga J, Bourne JR. Calculation of micromixing in inhomogeneous stirred tank reactors. *Chem Eng Res Des*. 1988;66:33-38.
10. Baldyga J, Bourne JR. Micromixing in inhomogeneous turbulence. *Chem Eng Sci*. 1988;43:107-112.
11. Baldyga J, Bourne JR. Effect of micromixing on parallel reactions. *Chem Eng Sci*. 1990;45:907-916.
12. Bourne JR, Gholap RV, Rewatkar VB. Influence of viscosity on the product distribution of fast parallel reactions. *Chem Eng J/Biochem Eng J*. 1995;58:15-20.
13. Bakker RA, van den Akker HEA. A Lagrangian description of micromixing in a stirred tank reactor using 1D-micromixing models in a CFD flow field. *Chem Eng Sci*. 1996;51:2643-2648.
14. Akiti O, Armenante PM. A computational and experimental study of mixing and chemical reaction in a stirred tank reactor equipped with down-pumping hydrofoil impeller using a micro-mixing-based CFD model. *Proceedings of 10th European Conference on Mixing, Delft, The Netherlands, July 2–5, 2000*. New York, NY: Elsevier; 2000:61-68.
15. Uehara-Nagamine E, Armenante PM. Effect of process variables on the single-feed semibatch precipitation of barium sulphate. *Chem Eng Res Des*. 2001;79:979-988.
16. Tang L, Wen F, Crowe CT, Chung JN, Troutt TR. Self-organizing particle dispersion mechanism in a plane wake. *Phys Fluids A*. 1992;4:2244-2251.
17. Yang Y, Crowe CT, Chung JN, Troutt TR. Experiments on particle dispersion in a plane wake. *Int J Multiphase Flow*. 2000;26:1583-1607.
18. Chein R, Chung JN. Simulation of particle dispersion in a two-dimensional mixing layer. *AIChE J*. 1988;34:946-954.
19. Froncioni AM, Muzzio FJ, Peskin RL, Swanson PD. Chaotic motion of fluid and solid particles in plane wakes. *Chaos Soliton Fract*. 1997;8:109-130.
20. Roizard C, Poncin S, Lapicque F, Py X, Midoux N. Behaviour of fine particles in the vicinity of a gas bubble in a stagnant and a moving fluid. *Chem Eng Sci*. 1999;54:2317-2323.
21. van der Zon M, Thoolen H, Hamersma PJ, Poels EK, Bliek A. Agglomeration and adhesion of catalyst particles in gas–liquid reactors. *Catal Today*. 2001;66:263-270.
22. Brilman DWF, Goldschmidt MJV, Versteeg GF, van Swaaij WPM. Heterogeneous mass transfer models for gas absorption in multiphase systems. *Chem Eng Sci*. 2000;55:2793-2812.

23. Liu S, Masliyah JH. In: Schramm LL, ed. *Rheology of Suspensions*. Washington, DC: American Chemical Society; 1996:107-176.
24. Maxey MR, Riley JJ. Equation of motion for a small rigid sphere in a nonuniform flow. *Phys Fluids*. 1983;26:883-889.
25. Coimbra CFM, Rangel RH. General solution of the particle momentum equation in unsteady Stokes flow. *J Fluid Mech*. 1998;370:53-72.
26. Fletcher CAJ. *Computational Techniques for Fluid Dynamics*. New York, NY: Springer-Verlag; 1997.
27. Deuflhard P, Hairer E, Zugck J. One-step and extrapolation methods for differential-algebraic systems. *Numer Math*. 1987;51:501-516.
28. Ehrig R, Nowak U, Oeverdieck L, Deuflhard P. In: Bungartz HJ, Durst F, Zenger C, eds. *High Performance Scientific and Engineering Computing*. New York, NY: Springer-Verlag; 1999:233.
29. Koynov A, Khinast JG. Effects of hydrodynamics and Lagrangian transport on chemically reacting bubble flows. *Chem Eng Sci*. 2004; 59:3907-3927.

Manuscript received Apr. 19, 2004, and revision received Oct. 13, 2004.